iScience

CellPress
OPEN ACCESS

Article

Deformation resilient cement structures using 3D-printed molds

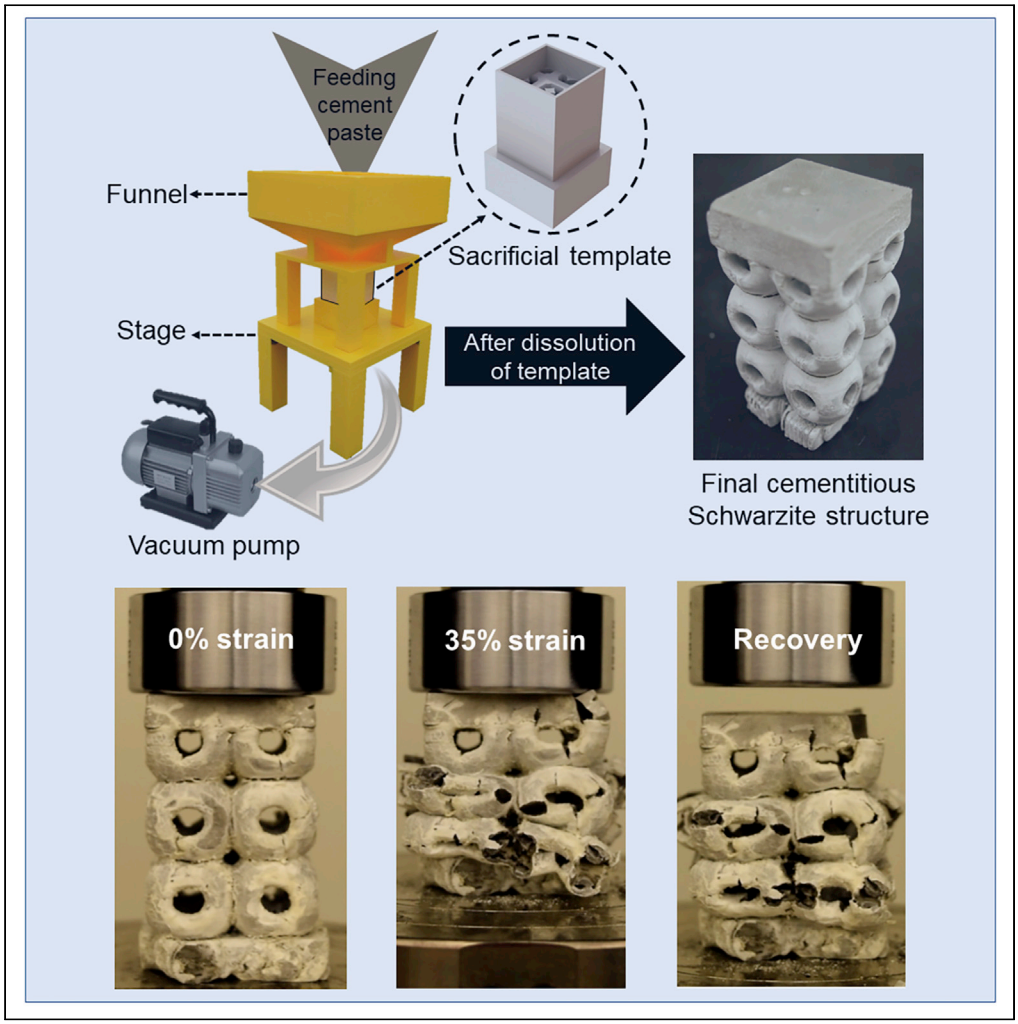

Seyed Mohammad Sajadi, Chandra Shekhar Tiwary, Amir Hossein Rahmati, ..., Muhammad M. Rahman, Ashokkumar Meiyazhagan, Pulickel M. Ajayan

peter.boul@aramcoservices.com (P.J.B.)
mr64@rice.edu (M.M.R.)
ma37@rice.edu (A.M.)
ajayan@rice.edu (P.M.A.)

HIGHLIGHTS

A polymer-coated architected cementitious structure is developed

Catastrophic failure is prevented through delayed damage propagation mechanisms

Significant structural recovery is observed after releasing compression loading

Sajadi et al., iScience 24, 102174
March 19, 2021
https://doi.org/10.1016/j.isci.2021.102174

iScience

CellPress
OPEN ACCESS

Article

Deformation resilient cement structures using 3D-printed molds

Seyed Mohammad Sajadi,[1] Chandra Shekhar Tiwary,[2] Amir Hossein Rahmati,[3] Shannon L. Eichmann,[4] Carl J. Thaemlitz,[4] Devashish Salpekar,[1] Anand B. Puthirath,[1] Peter J. Boul,[4,*] Muhammad M. Rahman,[1,5,*] Ashokkumar Meiyazhagan,[1,*] and Pulickel M. Ajayan[1,*]

SUMMARY

Cementitious structures exhibit high compression strength but suffer from inherent brittleness. Conversely, nature creates structures using mostly brittle phases that overcome the strength-toughness trade-off, mainly through internalized packaging of brittle phases with soft organic binders. Here, we develop complex architectures of cementitious materials using an inverse replica approach where a soft polymer phase emerges as an external conformal coating. Architected polymer templates are printed, cement pastes are molded into these templates, and cementitious structures with thin polymer surface coating are achieved after the solubilization of sacrificial templates. These polymer-coated architected cementitious structures display unusual mechanical behavior with considerably higher toughness compared to conventional non-porous structures. They resist catastrophic failure through delayed damage propagation. Most interestingly, the architected structures show significant deformation recovery after releasing quasi-static loading, atypical in conventional cementitious structures. This approach allows a simple strategy to build more deformation resilient cementitious structures than their traditional counterparts.

INTRODUCTION

The design and fabrication of lightweight structures with high stiffness and toughness remain a challenge since these properties are mutually exclusive (Studart, 2014; Zhang et al., 2016). However, nature excels in generating lightweight materials such as wood (Gibson, 2012) and bone (Reznikov et al., 2014; Sherman et al., 2015), etc. with such mechanical performances by combining different toughening mechanisms across multiple length scales (Wegst et al., 2015). This is achieved via autonomous hierarchical assembly and complex sequential architectures that are the two underlying features responsible for their exceptional mechanical performance (Aizenberg and Fratzl, 2009; Barthelat et al., 2007). The hierarchical arrangement of stiff and soft components spans from the sub-micron to the macro-scale with a highly oriented and compact packing that imparts toughness in many natural structures. Nacre is a well-studied example of this phenomenon (Gim et al., 2019; Greco et al., 2020). Although the soft internal interfaces are diminutive regarding volume fraction in these materials, they govern these materials' overall mechanical properties to a large extent. Aside from the structural hierarchies with internal interfaces, the complex geometric regularities witnessed in many natural structures often offer unique and exceptional mechanical properties (Mckittrick et al., 2010; Sajadi et al., 2019c), such as the hexagonal arrangement of honey hives (Corni et al., 2012) and spiral patterns in mollusks (Chen et al., 2012).

Cementitious materials, the most widely used structural materials in the world, do not benefit from pre-programmed failure mechanisms that hierarchically arranged and patterned natural materials possess. Thus, while they benefit from high compressive strength and high Young's modulus, cementitious materials typically display low plastic deformation and toughness. Solutions to these limitations and issues in brittleness can potentially be realized by mimicking hierarchical biological structures with diminutive internalized interfaces. Additive manufacturing provides the precision and accuracy required to architect biomimetic synthetic materials with geometrically organized layers and interfaces that are capable of built-in features, including controlled failure as observed in nature (Maguire et al., 2020; Sajadi et al., 2019b). However, the development of complex architected cementitious structures pre-programmed with controlled failure through 3D printing remains an elusive goal.

[1]Department of Materials Science and NanoEngineering, Rice University, Houston, TX 77005, USA

[2]Metallurgical and Materials Engineering, Indian Institute of Technology Kharagpur, Kharagpur, West Bengal, India

[3]Department of Mechanical Engineering, University of Houston, Houston, TX 77005, USA

[4]Aramco Americas, Houston, TX 77084, USA

[5]Lead contact

*Correspondence: peter.boul@aramcoservices.com (P.J.B.), mr64@rice.edu (M.M.R.), ma37@rice.edu (A.M.), ajayan@rice.edu (P.M.A.)

https://doi.org/10.1016/j.isci.2021.102174

Here, we report a simple fabrication method to develop a complex porous architecture of cementitious material with high stiffness and toughness using an inverse replica approach via solubilization of sacrificial templates. In this approach, an architected sacrificial polymer template is 3D-printed via fused-filament fabrication (FFF) technique, and the cement paste is poured into the template cavity. The inverse replica approach overcomes the physical, functional, and geometric limitations of other additive manufacturing techniques, such as direct ink writing (DIW), where rheology optimization, homogeneity, and microstructural control of cementitious materials is an issue (Khan et al., 2020; Moini et al., 2018). There are several efforts reported on DIW of cementitious materials that focused on resolving the technological challenges related with ink formulations and other rheological issues (Hambach and Volkmer, 2017; Khan et al., 2020; Moini et al., 2018; Perrot et al., 2016; Vergara and Colorado, 2020). However, the higher precision and accuracy in FFF of thermoplastic polymers, compared with DIW of cement paste, can be exploited to pattern highly accurate architectures of cementitious materials using 3D-printed polymer templates. Earlier, cementitious composites were developed by incorporating FFF-manufactured acrylonitrile butadiene styrene polymer structures inside a cement mortar cast (Askarinejad et al., 2018; Rosewitz et al., 2019) The positive effect of incorporating the cellular polymer phase in cementitious composites was observed clearly in the mechanical properties. All mechanical properties of composites with architected polymer structures were greater than those of control samples due to the interlocking elements and prevention of localized deformation and failure. Thus, this method overcomes the technical limitations of DIW of cementitious materials, precluding the need for stringent rheological requirements on the ink for cement writing (Sajadi et al., 2019a). Furthermore, the properties of the plastic template/mold at the interface with cementitious materials can greatly influence the mechanical properties of the composite even when much of the original mold is removed (i.e., through solubilization).

Our sacrificial template for the inverse replica approach was developed using polyvinyl alcohol (PVA) via the FFF technique. We selected primitive schwarzites as a complex architecture to produce a PVA template with multifaceted features, including shapes and curvature. Interestingly, while the polymer template provided precise geometrical shapes for the cement paste, the functional groups present in the cement interact with the polymers to form an interconnected robust polymer-cement interface in an externalized fashion contrary to natural materials. We analyzed the quasi-static mechanical behavior of such cementitious schwarzite structure with external PVA interfaces to investigate the failure mechanisms and compared to that of standard bulk (non-porous) cementitious structures. We also performed a comparative study using a continuum plasticity-based damage model to qualitatively investigate the effect of coating on damage initiation and propagation under compression load.

RESULTS AND DISCUSSION

Fabrication, morphology, and composition of cementitious schwarzites

Schwarzites are complex three-dimensional periodic structures formed based on the minimal surface that exhibit positive and negative Gaussian curvatures with tunable cell size and shape and unusual mechanical properties (Sajadi et al., 2018). As such, there is interest in adopting this geometry in macroscopic scales to develop superb energy-absorbing materials capable of withstanding large compressive forces. Earlier, geometrically optimized schwarzite structures with different cell size, shape, and numbers have been extensively studied at the molecular scale to understand their mechanical behavior and then, inspired from that, these geometries were 3D printed at the centimeter scale to analyze the macro-mechanical performance of polymer-based architected structures (Felix et al., 2020; Sajadi et al., 2018) Here, we selected an optimized schwarzite structure (primitive) as a model to understand the macro-scale mechanical behavior of such complex architected cementitious structure with a micro-scale polymer coating.

We have developed a PVA-based inverse replica of sacrificial templates using a high-resolution FFF 3D printer, and a positive replica or schwarzite has been developed by pouring cement paste into the template (See Transparent methods and Table S3 for details). PVA was used due to the hydrophilicity and owing to its easy removal in water since our technique for creating inverse replica architectures is achieved via solubilization of sacrificial templates. Figure 1A (i) shows a schematic of the setup with a water-soluble PVA template, which is filled with the cement slurry to attain a uniform cement distribution. A guided funnel facilitates the feeding process of cementitious materials, and a stage fixes the position during the fabrication process while a vacuum pump helps to achieve a uniform slurry distribution and assists in reducing voids. We observed that the cementitious schwarzite structures had no visible shrinkage after curing and were a closely accurate inverse replica of 3D-printed PVA templates by complete and homogeneous infiltration

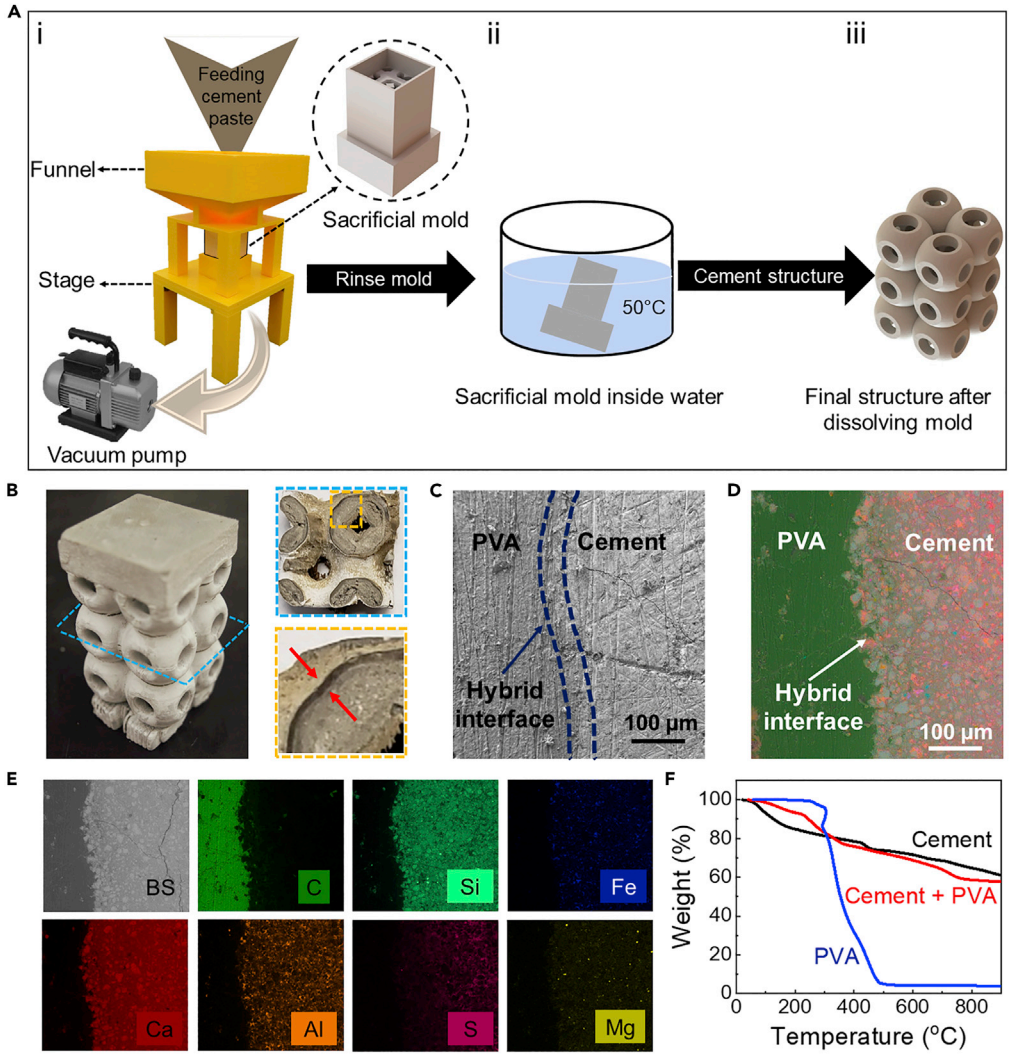

Figure 1. Fabrication, morphology, and composition of cementitious schwarzites

(A) Scheme showing development of the architected structures: (i) the printed PVA mold is filled with the cement paste via a guided funnel and vacuum pump assembly, (ii) after curing of the cement slurry inside the sacrificial template, the mold was immersed in hot water to dissolve the sacrificial template, and (iii) the rinsed, dried cementitious schwarzite structure with a thin PVA coating.

(B) Photographs of cementitious schwarzite structures prepared using inverse replica molding. Center part of the structure was sliced for morphological characterization.

(C) SEM image showing the cementitious material, PVA, and the hybrid interface in the architected structures.

(D) Backscatter SEM image overlaid with false-colored EDS elemental maps of the structure confirming the three different regions (cementitious material, PVA, and the hybrid interface).

(E) Backscatter and EDS elemental maps showing the presence of different elements such as C, Si, Fe, Ca, Al, S, and Mg on the surface of the cementitious structures.

(F) Thermogravimetric analysis of PVA, cementitious material, and hybrid interfaces.

under vacuum. Note that the cement slurry inside the sacrificial template was held and cured at consistent relative humidity and ambient temperature. Optimum curing time in a moist environment prevents drying shrinkage which occurs due to contraction of cement for moisture loss (Rosewitz et al., 2019). After curing the cementitious materials, the molds were immersed in hot water (~50°C) for 4 days to dissolve the sacrificial PVA template (Figure 1A (ii)). The solubilization process of the template removes most of the polymer except for a thin layer that coats the surfaces of the cementitious schwarzite structures. Even further treatments such as prolonged washing in hot water (~70°C) did not affect the coating on the surface of the

cementitious structure. We analyzed the samples with scanning electron microscopy (SEM) to investigate the topography and thickness of the coating onto the structures. Figure 1B confirms that a thin layer of PVA coated the whole surface. Also, we observed that PVA interacts strongly with the cement surfaces and fills the surface pores, thus generating a smooth hybrid interface region (Figures 1C and 1D). Note that for the case of chemically reactive polymers, like polyvinyl alcohol, the mechanism of the reaction is not yet completely understood due to the amorphous nature. However, discussions were made based on studies on microstructure and molecular structure, and it is proposed that calcium complexes are formed by chemical interaction between the hydroxyl (-OH) group in PVA with cement. Singh and Rai reported that the formation of some new compounds in PVA-modified cement paste (which could be due to the chemical interaction between cement and PVA) was observed under UV-visible spectra (Singh and Rai, 2001). Hence, we hypothesize that this hybrid region is also a result of strong adhesion of the polymer with the cement that could be attributed to the chemical interaction between the hydroxy (OH) group in PVA with the carboxylate (COO-) groups in the cement (Kim and Robertson, 1998; Mansur et al., 2007). As such, we observed an externalization of the soft coating entirely from the hard cement through a homogeneous chemical interlocking between the cement and polymer surfaces with no separated interfaces.

Next, we have investigated the PVA-cement interface of the developed schwarzite structures via SEM and energy dispersive spectroscopy (EDS) to understand the morphology and elemental composition. Figure 1B shows the photograph of the whole structure with a plane to indicate the cutting section of the structure for SEM analysis. Note that tool marks with some visible cracks were observed in the sample during sectioning. Figure 1D shows the backscatter image overlain with the false colored elemental maps shown in Figure 1E. The elemental maps include carbon (C), magnesium (Mg), aluminum (Al), silicon (Si), sulfur (S), calcium (Ca), and iron (Fe). The analyses clearly show that the coating layer is carbon rich as expected from the exterior coating of polymer, while the cement is an inorganic-rich composition (Figures 1E and S1).

We observed three different regions (Figures 1C and 1D) and classified them as (i) the pure cementitious, (ii) the hybrid interface (composite of PVA and cement paste), and (iii) the pure PVA regions. The overall thickness of the coating was found to be around 200 μm (Figure 1C). The hybrid interface (Figure 1D) shows the layover boundary separating the polymer and the cementitious phases, while the polymer fills the surface pores of the cementitious materials to form a uniform and homogeneous region.

We confirmed the hybrid interfaces by conducting thermogravimetric analysis (TGA) of the three regions separately (Figure 1F). The pure PVA region shows significant weight loss (~95%) between 300 and 550°C due to the complete thermal decomposition with an onset degradation temperature of ~300°C. On the contrary, four main thermogravimetric phenomena were observed in the derivative TGA (DTG) of cementitious materials (Figure S2A) (Alarcon-Ruiz et al., 2005; Soares et al., 2015). The first phenomenon corresponds to the weight loss due to the unbound water evaporation at 30–120°C. The second phenomenon corresponds to the dehydration at 120–300°C due to chemically bonded water loss in the slurry, including the decomposition of ettringite and hydrated calcium silicate. The third phenomenon corresponds to the de-hydroxylation of portlandite, which occurs at around 400–500°C. The decarbonation of calcium carbonate occurs between 600 and 900°C in the fourth phenomenon. Overall, the cementitious materials show around 40% weight loss at 900°C. In the case of hybrid interfaces, there are three main thermogravimetric phenomena (Figure S2B). The first phenomenon corresponds to the weight loss related to the unbound water evaporation from 30–120°C. Decomposition of PVA occurs between 250 and 400°C with an onset degradation temperature of around 300°C during the second phenomenon. A third onset degradation temperature is observed around 700°C which might be due to the decomposition of the chemically bonded hybrid interface.

Mechanical properties and fracture behavior

To understand the role of geometry, we developed a solid rectangular cementitious structure (~38 mm × 38 mm × 54 mm) using the same composition and similar curing procedure followed in case of cementitious schwarzite structures. We compared the mechanical response of the solid block with the schwarzite structure in uniaxial compression mode (Figures 2A and 2C). We measured the specific energy absorption of each structure in compression mode by taking into consideration their weight. The schwarzite structure displayed significantly higher specific energy absorption (~0.6 J/g) compared to the standard cementitious structure (~0.27 J/g) (Figure 2A). Consequently, the schwarzite structure displayed significant improvement (~17 times higher) in fracture strain compared to the rectangular block prepared using the conventional

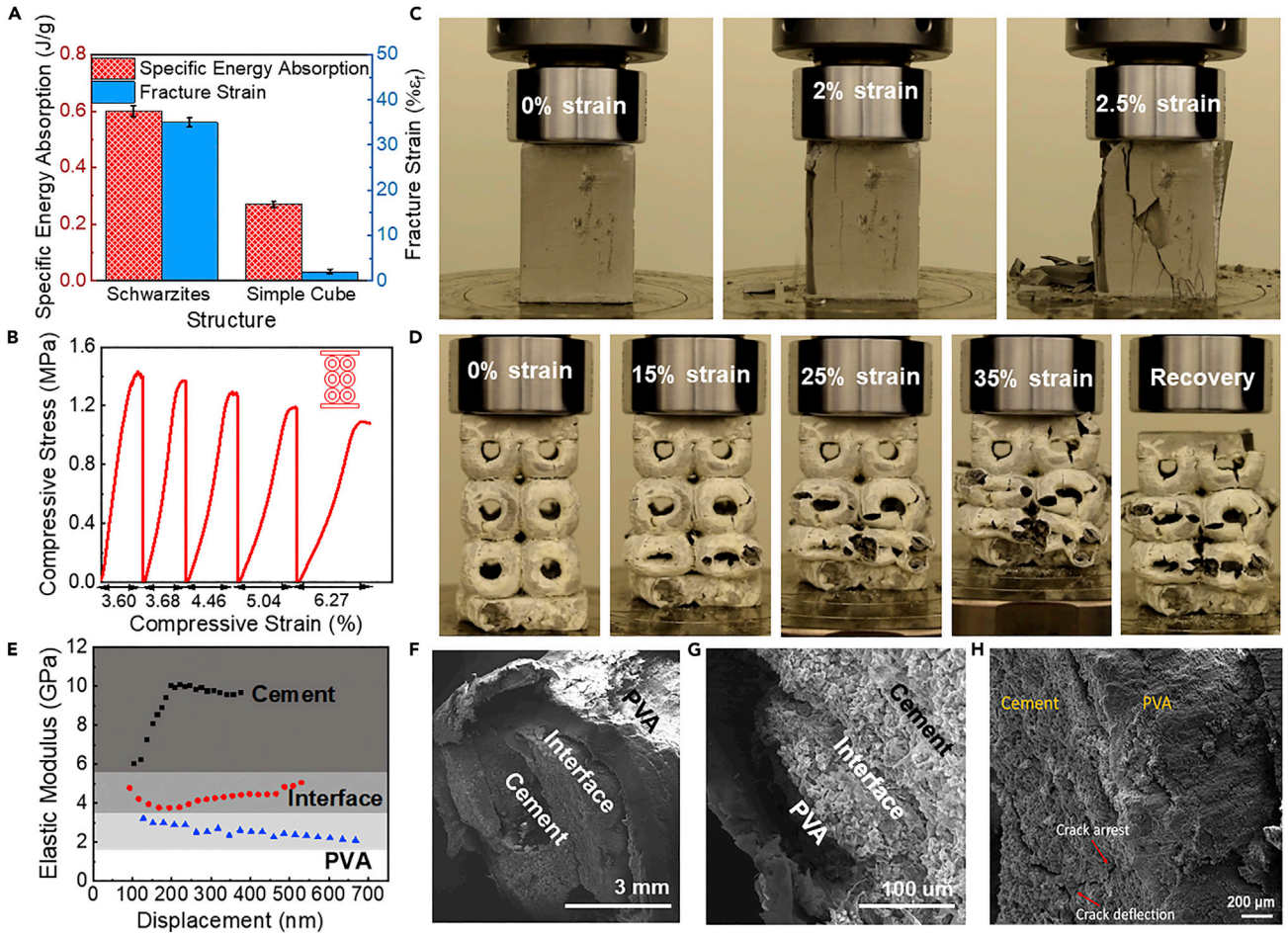

Figure 2. Mechanical properties and fracture behavior

(A–D) (A) Specific energy absorption and fracture strain for different structures, Data are represented as mean ± standard deviation (SD). (B) dynamic compressive stress *vs.* strain studies on a sample in different strain levels (see also Video S2). Crack propagation as a function of load shows the (C) catastrophic cracking at a minimal strain in the vertical shear direction of rectangular cementitious structure, (D) schwarzite structure illustrates compartmentalized crack propagation in the horizontal direction and deformation resiliency after unloading (see also Video S1).

(E) Micromechanical properties of the PVA, hybrid interface, and cementitious material region of schwarzite structure based on the nanoindentation mapping.

(F–H) SEM images of the surface topography at different magnifications. (F) The fracture surface of the cementitious schwarzite structure with the PVA layer. The scale bar is 3 mm.

(G) The three different regions in the fracture surface of the structure are shown. The scale bar is 100 μm.

(H) Magnification of the fracture surface in the hybrid region shows how the interface arrested and deflected the crack and delayed propagation. The scale bar is 200 μm.

casting technique. The typical brittle mechanical behavior was clearly observed in the solid cementitious structure. However, part of the toughening effect, as observed in the schwarzites, is due to the presence of geometric porosity in the structure (Figure S3). To understand the general applicability of coating irrespective of underlying cementitious structures based on different geometries, we developed solid rectangular cementitious structures with coating in the similar process. We conducted compression tests on solid structures with coating and observed a distinct improvement in the fracture strain (~2.5 times higher) and toughness (~1.5 times higher) of coated solid structures compared to the uncoated counterpart (Figure S4). While the effect of coating is obvious in the dense structures, we observe a significant benefit of the effect of coating in architected structure. Architected schwarzite structures with coating show much larger differences in toughness and fracture strain due to their higher surface area coating compared to the uncoated and coated solid structures. Most interestingly, we observed a geometric deformation recovery upon releasing the stress after compression testing, and the structure was trying to spring back to its original shape with some plastic deformation or damage (Video S1). To understand the structural recovery or elastic

behavior of the whole structure when releasing the compressive stress, we carried out a dynamic test on the schwarzite sample and applied cyclic compression strain on the sample and measured the stress (Figure 2B). At 3.6% strain, the structure springs back to its original shape upon releasing the applied load. This is very unlikely in conventional cementitious structures, which fail catastrophically at much earlier deformation (~2% strain). We repeated the cyclic strain up to five cycles, and the structure did not collapse, although we observed progressively nonlinear elastic responses in each subsequent cycle, which refers to some plastic deformation or damage in the progression of each cycle (Figures 2B and Video S2).

A series of snapshots were taken at different strain ranges to understand the macroscopic deformation mechanism of these structures (Figures 2C and 2D). Since cementitious material is inherently brittle, the solid cementitious structure failed catastrophically at a low strain level (~2%). Macro-scale cracks originated and propagated very quickly through the entire structure leading to complete fracture. However, the schwarzite structures displayed fractures more in a ductile mode with the progressive crushing of the unit cells (Figure 2D). We observed fine microcracks on the surface of the individual cells, but the complete structure did not disintegrate, as seen in the solid cementitious structure. The progressive load failure mechanisms are attributed to the compartmentalization of forces from the load-bearing components resulting in controlled failure (Figure S3). The fracture strain of the schwarzite structure was found to be around 35%, which is a significant enhancement for cementitious materials. This proves the synergistic role of the architecture and coating, which helps in strain distribution and thereby results in a higher strain to failure. The complex schwarzite architecture consists of positive and negative curvatures, which results in stress/strain delocalization, leading to preferential deformation and crack diversion/restriction in the sample.

Aside from the geometry role, another factor contributing to the enhanced toughness of the schwarzites is the considerable effect of the polymer micro-coating on the cement surface. As a surface coating, the polymer fills the micropores in the exposed surfaces of the cementitious structure and creates a uniform interlocking via chemical interaction in the cementitious material-PVA interfaces, which facilitates crack arrest and deflection in the interfaces during fracture after initiation from the cementitious phases. SEM analysis was conducted on the fracture surface of the schwarzite structure to understand these mechanisms (Figures 2F–2H). The lower magnification SEM image displays three regions as identified by cementitious, PVA, and hybrid interface region (Figures 2F–2H). Figure 2H shows the interface region delayed propagation of the crack through arresting and deflection. The soft polymer diverts the crack and results in higher fracture strain. The crack originating from the core reaches the near-surface polymer film and starts diverging, resulting in high specific fracture energy. The PVA coating can be stretched upon crack opening along the wake of the crack and resists the crack growth by reducing local stresses at the tip. In order to correlate the macroscopic deformation with the mechanical properties of the microscopic regions, we carried out nanoindentation studies on the developed schwarzite structure at these three different regions. The nano-indentation mapping over each region displays significantly different micromechanical properties (Figures 2E and S5). The PVA region showed a calculated reduced modulus of around 2.54 $\pm$ 0.31 GPa, while the cementitious region showed the modulus of ~9.09 $\pm$ 1.24 GPa. The hybrid interface displayed a modulus value of about 4.33 $\pm$ 0.37 GPa. The intermediate modulus value indicates the formation of a new region due to the chemical interactions between PVA and cement (Hu and Li, 2015). The controlled failure behavior could originate partly from the progressively decreased modulus value along the cementitious to PVA region.

Finite element analysis of cementitious schwarzites

Numerical failure analyses were carried out on a simple unit cell of schwarzite structure to qualitatively investigate the effect of a thin layer of PVA on damage propagation using the finite element model (FEM). The constitutive response of the cementitious materials is modeled using the combined plasticity-damage law. We calibrated the damage evolution model and plasticity properties of the material in a way that failure of the unit cell made of pure cementitious structure occurs at about 1.5% strain (Figure 3A). The strain level was determined based on experimental observation of the plastic deformation of cementitious structures that started at 1.5% strain. Then, we added the thin hybrid interface (consisting of polymer and cementitious materials) to the same model and compared damage propagation in the presence and absence of the hybrid interface (Figure 3Bi). The thickness of the hybrid interface is selected based on the SEM measurements, and the elastic modulus is acquired from nano-indentation studies. (Details of FEM models are explained in Methods, Figure S6, Tables S1 and S2, and Videos S3 and S4). The

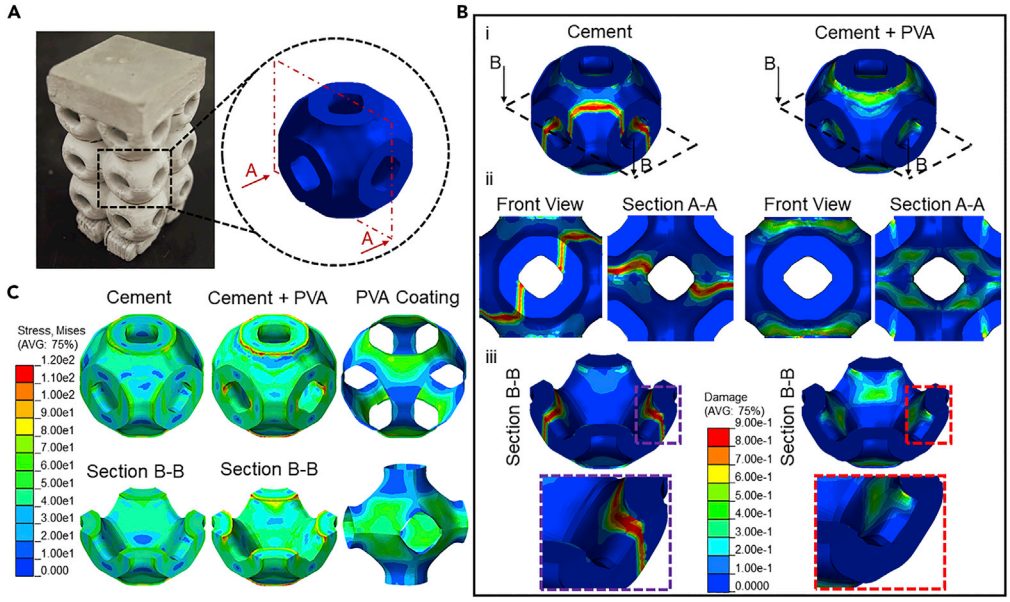

Figure 3. Finite element analysis of cementitious schwarzites in plastic region

(A) Photograph of the schwarzite structure developed using the sacrificial mold. The dotted line shows the unit cell used to design the model for FEM studies. For better presentation, the unit cell was sectioned from the middle.

(B) The finite element simulation on the unit cell of primitive schwarzite with and without coating in the plastic region. Damage contours for coated and uncoated samples are shown (i). To better demonstrate the role of the coating, the stress distribution is shown in the section view in both structures under the same boundary conditions (ii-iii). Damage in cementitious materials is considerably greater than that in the cement with PVA.

(C) The stress distributions in the same region of cement, cement with PVA coating, and coated PVA are plotted under the same amount of force.

See also Tables S1 and S2, Figure S6, and Videos S3 and S4.

static and cyclic model studies were carried out in the plastic region with the same boundary conditions as used for the uniaxial compression test. Figure 3B shows the damage contours in both structures (cementitious alone and cementitious with PVA coating structure). The damage variable can take values from zero, representing the undamaged material, to one, which represents the total loss of strength. To simplify the convergence of the numerical solution, we have set the maximum damage variable to be 0.9 instead of 1.0. In order to alleviate potential spurious mesh sensitivity issues induced by strain softening, the element sizes between the models are kept the same.

The schwarzite structure with the hybrid surface (Figure 3Bi-iii) shows the damage is significantly lower in the cementitious structure coated with PVA compared to the uncoated sample. A damage path is seen in the uncoated cementitious sample, which divides the specimen into two parts throughout the thickness of the sample resulting in brittle failure. On the contrary, the cementitious structure with a hybrid interface sample experiences far milder damage and plastic strain compared to the uncoated sample. For better representation, two-section views (A-A and B-B) and magnified regions were employed (Figure 3B ii-iii); red illustrates the crack region, which is already in the plastic zone. With the same boundary condition, the coated sample has a much lower plastic strain compared to the uncoated sample. The cross-sectional view of the unit cell is shown as section A-A and section B-B, and it delivers a better view of the reduced damage experienced by the areas coated with PVA. The section views of a single unit cell and inside and outside the PVA coating (shown in Figure 3C) reveal the stress distributions experienced in both the structures under the same amount of total strain. The pure cementitious structure results in reduced stress at the surface (green color on the surface), which clarifies the damage and plastic deformation and releasing energy to the environment. The hybrid/interface zone shows a uniform and higher stress (red color on the tip), which indicates an increased toughness or higher fracture strain. The uniform stress distribution in the PVA coating inside and outside of the structure reveals the parts under compression (green) and tension (blue) in the coating. These observations are consistent with our fracture surface analysis. The

stress magnitude is plotted for both structures, which shows a similar path (Figure S6). From these results, we conclude that the PVA coating considerably delays damage propagation and structural failure.

Conclusions

We have developed complex schwarzite structures of cementitious materials with a thin PVA layer via inverse replica. The functional groups present in the cementitious materials interact with PVA to form an interconnected robust polymer-cement interface in an externalized fashion unlike natural materials. Surprisingly, the cementitious schwarzite structures display unusual mechanical behavior with considerably high toughness and controlled failure compared to standard solid cementitious structures. Complex geometry and conformal coating, together, drastically alter the deformation modes and the stress localization to avoid catastrophic failure. Most interestingly, the architected structure shows deformation recovery significantly after the release of quasi-static loading, atypical in cementitious materials. Thus, this work shows a new perspective to develop deformation resilient cementitious structures with high toughness and opens the possibility of complex architected porous materials with structures previously unrealizable. Due to lightweight and ductility of the architected structures, this concept, in a broader view, can be applied for developing construction buildings in architectural scale instead of conventional construction materials to design load bearing, seismic-resistant structures.

Limitations of the study

The influence of different architecture varying coating thickness needs to be further considered. Also, while extending our lab scale demonstration of complex cementitious structure to architectural scale becomes a challenging task, the process also involves sacrificial templates, which increases processing as well as post-processing steps involved.

Resource availability

Lead contact

Further information and requests for resources should be directed to and will be fulfilled by the lead contact, Muhammad M. Rahman (mr64@rice.edu).

Materials availability

This study did not generate new unique reagents.

Data and code availability

This study did not generate datasets or analyze codes.

METHODS

All methods can be found in the accompanying Transparent methods supplemental file.

SUPPLEMENTAL INFORMATION

Supplemental information can be found online at https://doi.org/10.1016/j.isci.2021.102174.

ACKNOWLEDGMENTS

The authors gratefully acknowledge Dr. Caglar Oskay from Vanderbilt University for assistance in this work. We would like to thank Qiushi Sun and Joshua Brothers from the Reservoir Engineering Technology team at the Aramco Americas, Houston, for providing CT images and guidance during SEM and EDS data collection, respectively. C.S.T. acknowledges AOARD (Grant No. FA2386-19-1-4039) and Ramanujan fellowship, India.The authors gratefully acknowledge financial support from the Aramco Services Company, United States (Grant Reference Number: 1137681).

AUTHOR CONTRIBUTIONS

M.M.R., C.S.T., A.M., and P.M.A. designed and coordinated the study. S.M.S. fabricated cement structures. D.S., S.L.E, A.H.R., and A.B.P. characterized the structures. S.M.S., C.S.T., M.M.R., A.M., P.J.B., and P.M.A cowrote the paper. M.M.R., C.S.T., P.J.B., C.J.T., and P.M.A. discussed the results and commented on the manuscript. M.M.R. and P.M.A. supervised the study.

DECLARATION OF INTERESTS

The authors declare no competing interests.

Received: July 28, 2020
Revised: January 5, 2021
Accepted: February 7, 2021
Published: March 19, 2021

REFERENCES

Aizenberg, J., and Fratzl, P. (2009). Biological and biomimetic materials. Adv. Mater. *21*, 387–388.

Alarcon-Ruiz, L., Platret, G., Massieu, E., and Ehrlacher, A. (2005). The use of thermal analysis in assessing the effect of temperature on a cement paste. Cement Concrete Res. *35*, 609–613.

Askarinejad, S., Choshali, H.A., Flavin, C., and Rahbar, N. (2018). Effects of tablet waviness on the mechanical response of architected multilayered materials: modeling and experiment. Compos. Structures *195*, 118–125.

Barthelat, F., Tang, H., Zavattieri, P.D., Li, C.M., and Espinosa, H.D. (2007). On the mechanics of mother-of-pearl: a key feature in the material hierarchical structure. J. Mech. Phys. Sol. *55*, 306–337.

Chen, P.Y., McKittrick, J., and Meyers, M.A. (2012). Biological materials: functional adaptations and bioinspired designs. Prog. Mater. Sci. *57*, 1492–1704.

Corni, I., Harvey, T.J., Wharton, J.A., Stokes, K.R., Walsh, F.C., and Wood, R.J.K. (2012). A review of experimental techniques to produce a nacre-like structure. Bioinspir. Biomim. *7*, 031001.

Felix, L.C., Woellner, C.F., and Galvao, D.S. (2020). Mechanical and energy-absorption properties of schwarzites. Carbon *157*, 670–680.

Gibson, L.J. (2012). The heirarchial structure and mechanics of plant materials. J. R. Soc. Interf. *9*, 2749–2766.

Gim, J., Schnitzer, N., Otter, L.M., Cui, Y., Motreuil, S., Marin, F., Wolf, S.E., Jacob, D.E., Misra, A., and Hovden, R. (2019). Nanoscale deformation mechanics reveal resilience in nacre of Pinna nobilis shell. Nat. Commun. *10*, 1–8.

Greco, F., Leonetti, L., Pranno, A., and Rudykh, S. (2020). Mechanical behavior of bio-inspired nacre-like composites: a hybrid multiscale modeling approach. Compos. Structures *233*, 111625.

Hambach, M., and Volkmer, D. (2017). Properties of 3D-printed fiber-reinforced Portland cement paste. Cem. Conc. Compos. *79*, 62–70.

Hu, C., and Li, Z. (2015). A review on the mechanical properties of cement-based materials measured by nanoindentation. Constr. Build. Mater. *90*, 80–90.

Khan, M.S., Sanchez, F., and Zhou, H. (2020). 3-D printing of concrete: beyond horizons. Cement Concrete Res. *133*, 106070.

Kim, J.H., and Robertson, R.E. (1998). Effects of polyvinyl alcohol on aggregate-paste bond strength and the interfacial transition zone. Adv. Cement Based Mater. *8*, 66–76.

Maguire, A., Pottackal, N., Saadi, M.A.S.R., Rahman, M.M., and Ajayan, P.M. (2020). Additive manufacturing of polymer-based structures by extrusion technologies. Oxford Open Mater. Sci. *1*, https://doi.org/10.1093/oxfmat/itaa004.

Mansur, A.A.P., Santos, D.B., and Mansur, H.S. (2007). A microstructural approach to adherence mechanism of poly(vinyl alcohol) modified cement systems to ceramic tiles. Cement Concrete Res. *37*, 270–282.

Mckittrick, J., Chen, P., Tombolato, L., Novitskaya, E.E., Trim, M.W., Hirata, G.A., Olevsky, E.A., Horstemeyer, M.F., and Meyers, M.A. (2010). Energy absorbent natural materials and bioinspired design strategies : a review. Mater. Sci. Eng. C *30*, 331–342.

Moini, M., Olek, J., Youngblood, J.P., Magee, B., and Zavattieri, P.D. (2018). Additive manufacturing and performance of architectured cement-based materials. Adv. Mater. *30*, 1–11.

Perrot, A., Rangeard, D., and Pierre, A. (2016). Structural built-up of cement-based materials used for 3D-printing extrusion techniques. Mater. Struct. *49*, 1213–1220.

Reznikov, N., Shahar, R., and Weiner, S. (2014). Bone hierarchical structure in three dimensions. Acta Biomater. *10*, 3815–3826.

Rosewitz, J.A., Choshali, H.A., and Rahbar, N. (2019). Bioinspired design of architected cement-polymer composites. Cem. Conc. Comp. *96*, 252–265.

Sajadi, S.M., Boul, P.J., Thaemlitz, C., Meiyazhagan, A.K., Puthirath, A.B., Tiwary, C.S., Rahman, M.M., and Ajayan, P.M. (2019a). Direct ink writing of cement structures modified with nanoscale Additive. Adv. Eng. Mater. *1801380*, 1–10.

Sajadi, S.M., Owuor, P.S., Schara, S., Woellner, C.F., Rodrigues, V., Vajtai, R., Lou, J., Galvão, D.S., and Tiwary, C.S. (2018). Multiscale geometric design Principles applied to 3D printed schwarzites. Adv. Mater. *1704820*, 1–8.

Sajadi, S.M., Owuor, P.S., Vajtai, R., Lou, J., Ayyagari, R.S., Tiwary, C.S., and Ajayan, P.M. (2019b). Boxception: impact resistance structure using 3D printing. Adv. Eng. Mater. *1900167*, 1–10.

Sajadi, S.M., Woellner, C.F., Ramesh, P., Eichmann, S.L., Sun, Q., Boul, P.J., Thaemlitz, C.J., Rahman, M.M., Baughman, R.H., Galvão, D.S., et al. (2019c). 3D printed tubulanes as lightweight hypervelocity impact resistant structures. Small *15*, 1–9.

Sherman, V.R., Yang, W., and Meyers, M.A. (2015). The materials science of collagen. J. Mech. Behav. Biomed. Mater. *52*, 22–50.

Singh, N.B., and Rai, S. (2001). Effect of polyvinyl alcohol on the hydration of cement with rice husk ash. Cement Concrete Res. *31*, 239–243.

Soares, L.W.O., Braga, R.M., Freitas, J.C.O., Ventura, R.A., Pereira, D.S.S., and Melo, D.M.A. (2015). The effect of rice husk ash as pozzolan in addition to cement Portland class G for oil well cementing. J. Pet. Sci. Eng. *131*, 80–85.

Studart, A.R. (2014). Turning brittleness into toughness. Nat. Mater. *13*, 433–435.

Vergara, L.A., and Colorado, H.A. (2020). Additive manufacturing of Portland cement pastes with additions of kaolin, superplastificant and calcium carbonate. Constr. Build. Mater. *248*, 118669.

Wegst, U.G.K., Bai, H., Saiz, E., Tomsia, A.P., and Ritchie, R.O. (2015). Bioinspired structural materials. Nat. Mater. *14*, 23–36.

Zhang, C., Mcadams, D.A., and Grunlan, J.C. (2016). Nano/micro-manufacturing of bioinspired materials: a review of methods to mimic natural structures. Adv. Mater. *28*, 6292–6321.

iScience, Volume *24*

Supplemental information

Deformation resilient cement structures using 3D-printed molds

Seyed Mohammad Sajadi, Chandra Shekhar Tiwary, Amir Hossein Rahmati, Shannon L. Eichmann, Carl J. Thaemlitz, Devashish Salpekar, Anand B. Puthirath, Peter J. Boul, Muhammad M. Rahman, Ashokkumar Meiyazhagan, and Pulickel M. Ajayan

Supplemental Information

Deformation Resilient Cement Structures using 3D-Printed Molds

Seyed Mohammad Sajadi, Chandra Shekhar Tiwary, Amir Hossein Rahmati, Shannon L. Eichmann, Carl J. Thaemlitz, Devashish Salpekar, Anand B. Puthirath, Peter J. Boul, Muhammad M. Rahman, Ashokkumar Meiyazhagan, Pulickel M. Ajayan

Supplemental Figures and Tables

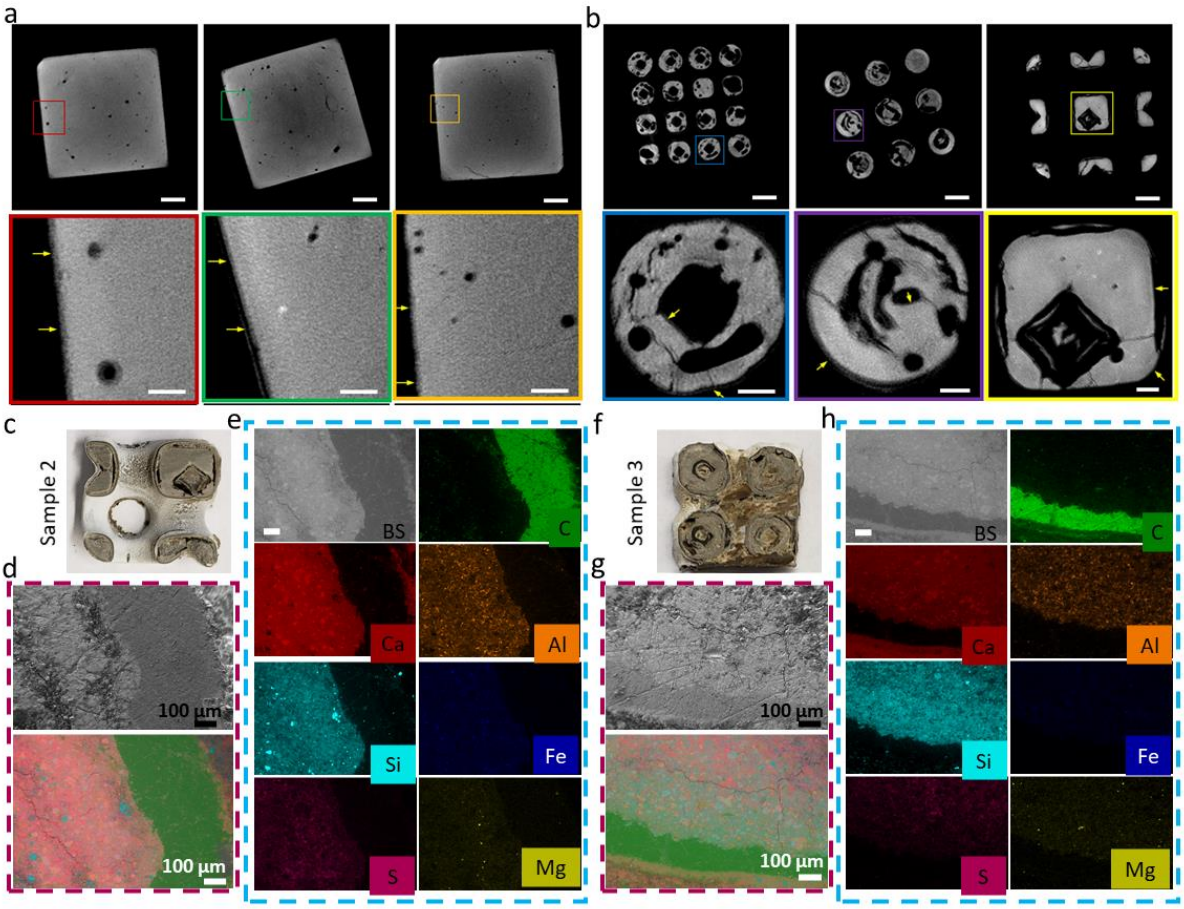

Figure S1. CT scan results (a-b) and SEM with EDS mapping (c-h) of the developed cement structure. Related to Figure 1e.

CT scans were collected to visualize the 3D cement structure and provide an initial check for polymer coating. Figure S1a-b shows representative slices from two locations. Figure S1a shows the rectangular cement block where the polymeric coating is along the outside of the cement with magnified images at the colored box. In these images, the darker gray region along the edge shows the polymeric coating. In each case, the slight grayscale variation along the edges of the cement indicates a polymeric coating. Figure S1b shows CT scan images from the regions of Schwarzite cementitious structures. From a qualitative overview using the images, the coating thickness varies from 100-200 µm. Given the low contrast and low resolution in these images, however, a quantitative measure of the layer thickness was not possible and SEM imaging with EDS mapping was used instead (Figure S1c-h). The bottom of Figure S1d and g show an overlay of the backscatter (BS) image with the C, Mg, Al, Si, S, Ca, and Fe elemental maps shown in Figure S1 e and h of sample 2 and 3 (Figure S1b top left and middle). It should be noted that the regions that are out of focus are detectable and, in some cases, visible in the EDS maps.

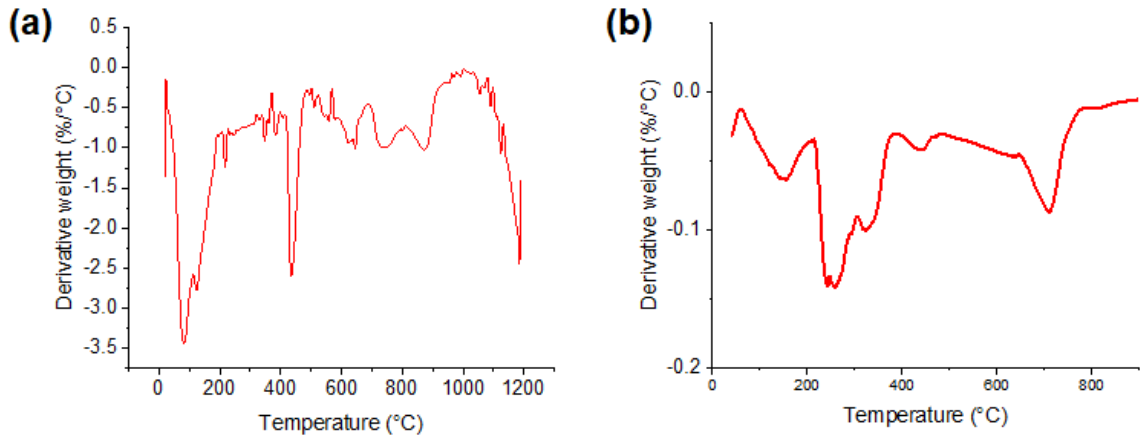

Figure S2. Derivative TGA of (a) cementitious materials and (b) hybrid interfaces. Related to Figure 1f.

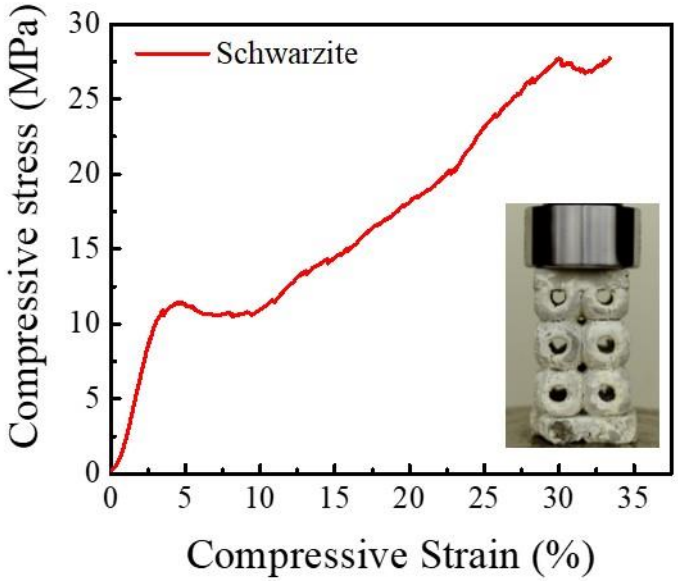

Figure S3. Typical compressive stress-strain behavior of cement in form of Schwarzites structure. The thin PVA layer coating-like effectively enhances the strength and toughness of the architected structure. The PVA coating is leading to a significant increase in the compressive toughness of the structure. As we can see the curve present three regimes i) a linear (elastic) region for compressive strains less than 5%; ii) a plateau (plastic) region beyond 5% followed by; iii) densification (nonlinear) which is the direct result of topology. Related to Figure 2d.

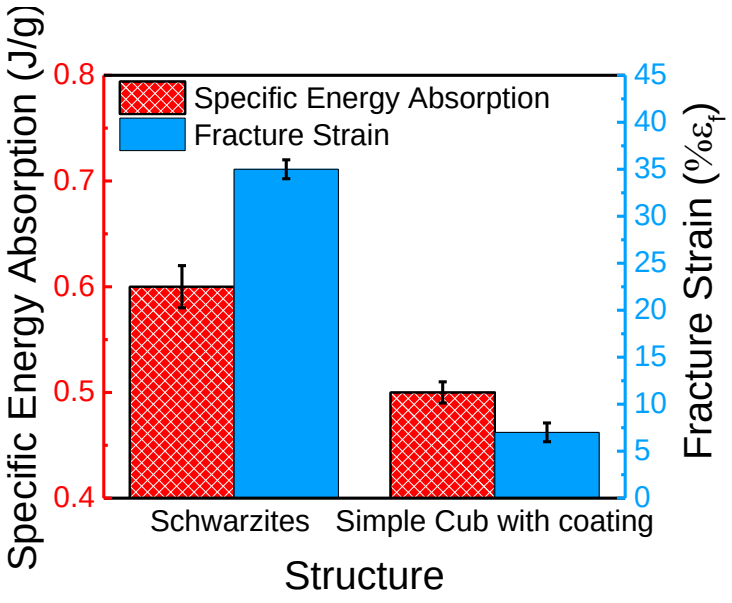

Figure S4. Specific energy absorption and fracture strain for PVA-coated Schwarzite and PVA-coated solid rectangular cementitious structures. Related to Figure 2.

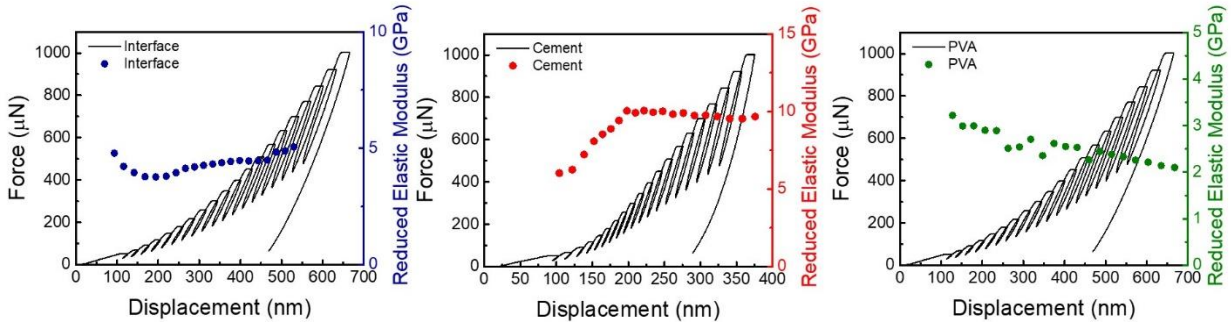

Figure S5. Nanoindentation results from the fracture surface of the Schwarzite structure, which shows there are three different regions. The reduced elastic modulus has a different value in the cement region, hybrid region, and PVA region, which indicate that we have an interface between PVA. Related to Figure 2e.

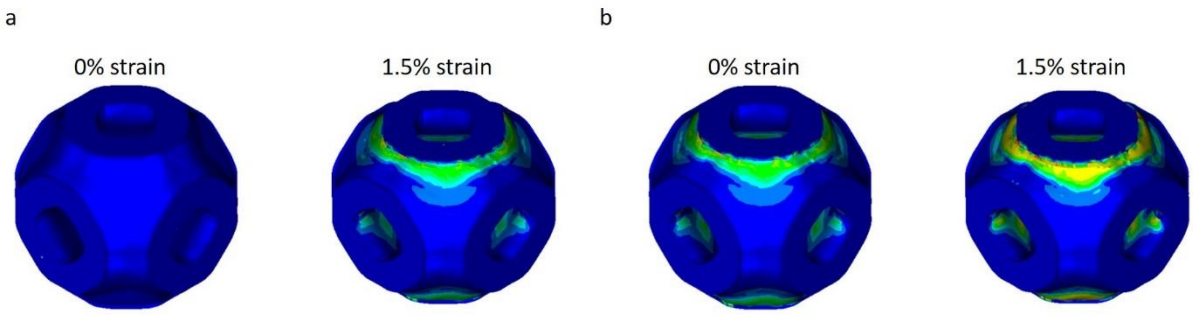

Figure S6. Cyclic simulation on cement with PVA coating. a) The damage contour on the first cycle at zero strain and 1.5%, which part of the sample experienced plastic deformation. b) In the next step, the load removed from the structure, and it recovered as a result of the elasticity of PVA. Then the load is applied again, and this time the structure experience more plastic deformation as it is shown in the figure. The structure has two parts the cement, which goes to the plastic region, and some energy dissipated and PVA coating, which deform, but it remains in the elastic region. Thus, by removing the load, the coating forces the structure to be recovered. Related to Figure 2b, Figure 3, and Video S4.

Table S1. The dimensionless yield stress in terms of in-elastic strain, related to Figure 3

$\bar{\sigma}_y$	ε_{in}
1	0
0.875	0.005
0.75	0.01
0.625	0.015
0.5	0.01
0.375	0.1
.25	1

Table S2. The degradation variable in terms of in-elastic strain, related to Figure 3

d	ε_{in}
0	0
0.2	0.01
0.6	0.02
0.8	0.05
0.9	0.05
0.9	1

Table S3. Parameter used for printing, related to Figure 1a

Parameter	**Value**
Nozzle temperature	200 ℃
Build plate temperature	55 ℃
Printing speed	50 mm/s
Layer height	100 µm
Filament cross-section	Zigzag

TRANSPARENT METHODS

Design of Schwarzite mold. A commercial water-soluble PVA filament (Ultimaker PVA, Young's modulus ~ 3.5 GPa, tensile strength ~ 80 MPa, and density ~ 1.23 g-cm^{-3}) with a diameter of 2.85 ± 0.10 mm was used to print the sacrificial molds. The 3D models of sacrificial molds were generated using SolidWorks and slic3r software was used to generate the G-code script. The molds were printed with a commercial FFF 3D printer (Ultimaker S3 Extended, USA) with a resolution of 10×10×20 μm in X, Y, and Z direction, respectively. PVA filaments were fed to into the printing head through a gear system guide and heated at a temperature of 200 °C (above the melting point of PVA). The melted PVA filament were extruded onto a build plate (temperature ~ 55 °C) through a brass nozzle with a diameter of 0.4 mm. The printing speed was maintained at 50 mm/s with layer height of 100 µm. **Table S3** shows all the parameters for printing the sacrificial PVA mold.

Cement paste preparation. Class G oil well cement was used in this study. It is commonly used for a wide range of downhole conditions. The chemical composition of Class G cement included 58% tricalcium silicate (C_3S), 19% dicalcium silicate (C_2S), 2% tricalcium aluminate (C_3A), and 11% tetracalcium aluminoferrite (C_4AF) (Kupwade-Patil et al., 2019). The fineness of this cement is 1400-1700 cm^2/g. The cement paste used in this study had a water-to-cement ratio of 0.45 by weight. The proper ratios of cement were added to water and mixed it with a constant speed mixer (Fann 686CS, Fann Instrument Company, USA) at 12000 rpm for 35 sec to obtain a homogeneous mixture according to ASTM C1738-Standard Practice for High-Shear Mixing of Hydraulic Cement Pastes. Finally, the mixture was used to fill the PVA template through a guided funnel feeding process using a vacuum pump.

Curing and storage of cementitious structures. Cement paste inside the sacrificial template was held and cured at ~100% relative humidity (RH) and ambient temperature (21 °C) for 3 days followed by immersing the sample for another 4 days in a 1L hot water bath (~50 °C) to dissolve the sacrificial PVA template. The samples were stored in a desiccator at 50% RH prior to mechanical testing. The final cementitious Schwarzite structures had a dimension of around 40 mm × 40 mm × 80 mm.

Characterizations. Scanning Electron Microscopy (SEM) and Energy Dispersive Spectroscopy (EDS) images were collected using a Zeiss Sigma HDVP (Zeiss, Inc., Germany) with a Bruker XFlash 6/30 SDD detector. To get a large field of view image that contained both the cementitious materials and coating, a relatively low-resolution Secondary Electron (SE) image was used with an accelerating voltage of 1 kV to produce a 750 x 1000 µm image, 3072 x 2304 pixels, at a pixel size of 325.5 nm/pixel. EDS maps, 1024 x 768 pixels of the same region as the SE images were collected at 976.5 nm/pixel using an accelerating voltage of 15 kV where the voltage was selected to produce sufficient counts on the spectrometer. During EDS acquisition, a backscatter (BS) image was collected along with elemental maps for aluminum (Al), carbon (C), calcium (Ca), chlorine (Cl), fluorine (F), iron (Fe), potassium (K), magnesium (Mg), nitrogen (N), sodium (Na), oxygen (O), phosphorous (P), sulfur (S), silicon (Si), and zinc (Zn). Not all elemental maps collected showed a contrast between the coating layer and cementitious material, and these data are not shown here.

The thermogravimetric analysis was carried out using Q-600 Simultaneous TGA/DSC from TA Instruments. About 10 mg of the sample was heated under an argon atmosphere at a heating rate of 20 °C/min from 30 to 900 °C. Uniaxial compressive tests were carried out at room temperature with an Instron 4505. The load was measured during compression, while the displacement of the crosshead was recorded. Nanoindentation studies were carried out under room temperature conditions. A Hysitron TI 980 Tribo Indenter, having Berkovich probe with a radius of curvature of 150 nm, was used for the nanoindentation measurements. A standard quasi load function with a maximum load of 1000 µN is employed for the single indentation test, and XPM mode with 1000 µN as maximum force is used for the accelerated property mapping over a given area. A minimum of three specimens from each category were tested to ensure the consistency of the data for all mechanical characterizations and an average value along with the standard deviation has been provided.

Finite element method. Finite element simulations are performed using the commercial code Abaqus to qualitatively investigate the effect of the coating on the failure behavior of the cementitious structure. For this purpose, we consider both damage and plasticity for the cement part and assign material properties in such a way that failure occurs at a strain of 1.5%. Then we add a thin membrane of coating to the material and compare its behavior with the material without coating. Such a comparative study can qualitatively show the effectiveness of the coating on changing the mechanical behavior of the material.

Standard implicit analysis with linear response for the elastic behavior of materials is employed. The materials have been assumed to be perfect and free of any defects in the undeformed configuration. The unit cells were discretized using linear tetrahedral elements with an approximate element size of 0.34 mm (the overall unit cell size is 20 mm). We set the elasticity modulus of cement to 9 GPa and Poisson's ratio of 0.14 based on experimental results. Also, we assume that the coating behaves linear elastic with an elastic modulus of 3 GPa and Poisson's ratio of 0.3 with a thickness of 200 μm. The nonlinear effects, plasticity, and damage in the coating is assumed to be negligible but both plastic and degradation behavior of cementitious material has to be included in the model. A concrete damage-plasticity (CDP) model is used to simulate the behavior of cementitious materials. The CDP model first presented by Lubliner and coworkers[49] and later modified by Lee and Fenves[50] is primarily intended to analyze concrete structures but is also suitable to study semi-brittle materials including ceramics (Simulia, 2016). In this model, damage in the material is quantified with compressive and tensile damage parameters which are denoted by d_c and d_t, respectively. Both these damage variables take values between zero and one where zero represents material is undamaged and one means total loss of strength. Total damage of the material is specified by $d = (1 - d_t)(1 - d_c)$. As the material degrades the elastic modulus of the material decreases. Therefore, the damaged elasticity equations are expressed as

$$\boldsymbol{\sigma} = (1 - d_t)(1 - d_c)\mathbf{C}(\boldsymbol{\varepsilon} - \boldsymbol{\varepsilon}^{\mathrm{p}}),$$

where $\boldsymbol{\sigma}$, $\mathbf{C}$, $\boldsymbol{\varepsilon}$ and $\boldsymbol{\varepsilon}^{\mathrm{p}}$ are, respectively, stress, elasticity tensor, total strain, and plastic strain. The reader is referred to Abaqus user's manual[51] for more information on the model. Dilation angle and flow potential eccentricity are two input parameters of models that are used in the flow potential function, which is the Drucker-Prager hyperbolic function. Values of 31° and 0.1 have been assumed for dilation angle and flow potential eccentricity, respectively. The yield function used in the model is the yield function presented by Lubliner et al.[49] modified by Lee and Fenves.[50] The shape factor and the ratio of biaxial to uniaxial compressive strengths are two input parameters

of yield function. Values of 0.66 and 1.16 have been considered, respectively, for the shape factor and ratio of biaxial to uniaxial compressive strength. Furthermore, considered values of yield stress and damage variable in terms of inelastic strain have been listed in Table S1 and Table S2, respectively, where $\bar{\sigma}_y = \frac{\sigma_y}{\sigma_{0y}}$, σ_y is yield stress and $\sigma_{0y} = 40$ MPa and we have assumed similar yield and damage behavior in tension and compression. As the objective of current analysis is not to investigate strength of cement specimen itself, current model and material properties have been considered in order to ensure failure in the cement specimen occurs in the total strain of about 1.5%, where total strain is defined as the total change in the height of unit cell divided by its initial length. This is consistent with our experimental observations. The objective of the current analysis is to qualitatively investigate the effect of the coating on the failure of the structure and no qualitative change will be observed in the presented results upon change of input parameters of the model although results may vary quantitively.

SUPPLEMENTAL REFERENCES

Kupwade-Patil, K., Boul, P.J., Rasner, D.K., Everett, S.M., Proffen, T., Page, K., Ma, D., Olds, D., Thaemlitz, C.J., Büyüköztürk, O., 2019. Retarder effect on hydrating oil well cements investigated using in situ neutron/X-ray pair distribution function analysis. Cement and Concrete Research 126, 105920. https://doi.org/10.1016/j.cemconres.2019.105920

Simulia, 2016. ABAQUS 6.14 user's manuals. Dassault Systèmes Simulia Corp 2016.